

Three months of local sea level derived from reflected GNSS signals

J. S. Löfgren,¹ R. Haas,¹ H.-G. Scherneck,¹ and M. S. Bos²

By receiving Global Navigation Satellite System (GNSS) signals that are reflected off the sea surface, together with directly received GNSS signals (using standard geodetic-type receivers), it is possible to monitor the sea level using regular single difference geodetic processing. We show results from our analysis of three months of data from the GNSS-based tide gauge at the Onsala Space Observatory (OSO) on the west coast of Sweden. The GNSS-derived time series of local sea level is compared with independent data from two stilling well gauges at Ringhals and Gothenburg about 18 km south and 33 km north of OSO, respectively. A high degree of agreement is found in the time domain, with correlation coefficients of up to 0.96. The root-mean-square differences between the GNSS-derived sea level and the stilling well gauge observations are 5.9 cm and 5.5 cm, which is lower than for the stilling well gauges together (6.1 cm). A frequency domain comparison reveals high coherence of the data sets up to 6 cycles per day, which corresponds well to the propagation of gravity waves in the shallow waters at the Kattegatt coast. Amplitudes and phases of some major tides were determined by a tidal harmonic analysis and compared to model predictions. From the GNSS-based tide gauge results we find significant ocean tidal signals at fortnightly, diurnal, semi-diurnal, and quarter-diurnal periods. As an example, the amplitudes of the semi-diurnal M_2 and the diurnal O_1 tide are determined with 1σ uncertainties of 11 mm and 12 mm, respectively. The comparison to model calculations shows that global ocean tide models have limited accuracy in the Kattegatt area.

1. Introduction

The impact of global warming and rising sea level is especially of interest for the human populations living in coastal regions and on islands. These areas are highly exposed to extreme weather such as storms, extreme waves, and cyclones, which does not only impact the population of these societies, but also their economy [Nicholls *et al.*, 2007]. One example is that from 1980 to 2000, about 250 000 people were killed in tropical cyclones. With an anticipated sea-level rise, the occurrences of these extreme events are increasing [Bindoff *et al.*, 2007]. It is therefore crucial for the safety of the population in these affected areas to monitor sea level and to increase the

understanding of the local hydrodynamic and meteorological response to a global sea-level rise.

Measurements from tide gauges provide sea level with respect to the land on which they are established, i.e., measurements of the vertical distance between the sea surface and the land surface, related to the Earth's crust. The resulting entity of local sea level is then directly related to the volume of the ocean.

In order to measure the sea-level change due to ocean water volume and other oceanographic change, all types of land motion need to be known. Global isostatic adjustment can be predicted from global geodynamic models [Bindoff *et al.*, 2007], but estimation of other reasons of land motions is not that well known and instead there is need for nearby geodetic or geological data. However, such datasets are not always available, resulting in inaccurate inference of sea level at sites with major tectonic activity. Thus, these sites are often removed from the overall sea-level analysis.

Satellite techniques, e.g., Global Navigation Satellite Systems (GNSS) can be used to measure land

¹Department of Earth and Space Sciences, Chalmers University of Technology, Gothenburg, Sweden.

²CIMAR/CIIMAR, Centro Interdisciplinar de Investigação Marinha e Ambiental, Universidade do Porto, Porto, Portugal.

motion, see e.g., *Lidberg et al.* [2010] and *Scherneck et al.* [2010]. Furthermore, the use of GNSS signals for remote sensing of the oceans were introduced by *Martin-Neira* [1993] with the PASSIVE Reflectometry and Interferometry System (PARIS). Land-based GNSS measurements of sea level and its variations due to tides has been carried out with interferometric techniques using code measurements, e.g., *Anderson* [2000], and phase measurements, e.g., [*Capparrini et al.*, 2007], and with customized receivers e.g., *Belmonte Rivas and Martin-Neira* [2006]. Additionally, aircraft ocean altimetry using GNSS signals have been performed, e.g., *Lowe et al.* [2002b], and space-based measurements of reflected GNSS signals, see *Lowe et al.* [2002a] and *Gleason et al.* [2005].

Recently *Löfgren et al.* [2010] and *Löfgren et al.* [2011] presented the concept of a GNSS-based tide gauge for observations of local sea level. Two standard geodetic-type GNSS receivers are used to receive direct GNSS signals through a zenith-looking Right Hand Circular Polarized (RHCP) antenna and GNSS signals reflected from the sea surface through a nadir-looking Left Hand Circular Polarized (LHCP) antenna. The carrier phase delay data from the receivers can be processed using relative positioning and standard geodetic analysis to obtain measurements of local sea level and sea level with respect to the Earth's center of mass, as realized by the GNSS systems. A similar technique was also used by *Martin-Neira et al.* [2002].

The advantage of this technique is that it allows to measure both sea surface height changes (relative positioning) and land surface height changes (e.g., precise point positioning, *Zumberge et al.* [1997]). Additionally, the combined measurements of local sea level are automatically corrected for land motion. This means that the GNSS-based tide gauge could, e.g., provide continuously reliable sea-level estimates in tectonic active regions. Furthermore, the geodetic analysis of the GNSS phase data promises a high accuracy.

The GNSS-based tide gauge was installed at the Onsala Space Observatory (OSO), on the west coast of Sweden, in the middle of September 2010. Since then, it has been continuously recording GNSS signals at 1 Hz. In our work, we present results from the first three months (95 days) of measurements. After a review of the technique (see Section 2 and Section 3), the GNSS data processing is explained together with the acquisition of sea-level time series (see Section 4). The GNSS-derived sea level is there-

after compared and evaluated against independent sets of sea level in both time and frequency domain (see Section 5 and Section 6).

2. Concept

The concept builds upon bistatic radar measurements at L-band to estimate the local sea level [*Löfgren et al.*, 2011]. Each GNSS satellite broadcasts carrier signals that are received both directly and after reflection off the sea surface (see Fig. 1). Two standard geodetic-type two-frequency GNSS receivers are used to track both the direct and the reflected signal. These data are analyzed in post-processing, using Global Positioning System (GPS) L_1 phase delays, to retrieve the sea-level information (see Section 4).

The installation of the GNSS-based tide gauge consists of two antennas mounted back-to-back on a beam stretching out over the coast line. One of the antennas is RHCP and zenith-looking, whereas the other antenna is LHCP and nadir-looking. The upward-looking antenna receives the GNSS signals directly and is used the same way as, e.g., an International GNSS Service (IGS) station. By solving for the position of this antenna, the land surface height with respect to the Earth's center of mass is obtained. The downward-looking antenna, on the other hand, receives the GNSS signals that have been reflected off the sea surface (when the GNSS satellites' RHCP signals reflect off the sea surface they change polarization to LHCP, see Section 2.1). Since the reflected signals travel an additional path, as compared to the directly received signals, the downward-looking antenna will appear to be a virtual RHCP antenna located below the sea surface. This virtual antenna will be at the same distance below the sea surface as the actual LHCP antenna is located above the sea surface, see Fig. 1. When there is a change in the sea surface, the additional path delay of the reflected signals changes, hence the LHCP antenna appears to change its vertical position. This means that the height of the downward-looking antenna over the sea surface (h) is directly proportional to the sea surface height with respect to the Earth's center of mass. From the geometry in Fig. 1, h can easily be related to the vertical baseline between the two antennas (Δv) according to

$$\Delta v = 2h + d \quad (1)$$

where d is the vertical separation of the phase centers of the two antennas. Thus, by combining the RHCP measurement of land surface height with the LHCP measurement of sea surface height, local sea level can be obtained.

Note that it is assumed that the phase centers of the antennas are aligned horizontally or that the horizontal distance is known and corrected for, which results in only a vertical difference between the antennas.

The manufacturer Leica Geosystems (Leica) could not provide us with information on the LHCP antenna's phase center variations. Therefore, as a first guess, we assume that the phase center variations of the LHCP antenna are identical to those of the RHCP antenna and the difference in phase center variations can be calculated. Since the LHCP antenna is downward-looking, the phase center variations will be mirrored in azimuth as compared to the upward-looking antenna. The difference in phase center variations was calculated using the absolute phase center corrections from IGS [Dow *et al.*, 2009] for the Leica AR25 multi-GNSS choke-ring antenna and the result is presented in Fig. 2. As can be seen, there is a clearly visible azimuth dependence for elevations below 40° . However, the range is never more than 2.5 mm and should not have a big impact on the final results.

2.1. Signal polarization

In order to investigate the effect of reflection in sea water on RHCP signals we use the Fresnel reflection coefficients for specular reflection, see e.g. [Rees, 2003]. The coefficients are complex valued and depend on the electrical properties of the reflecting surface (the dielectric constant and the conductivity of the reflecting medium) and the elevation angle of the incoming wave. By specifying these values it is possible to define the amplitude and phase of all kinds of polarization.

Fig. 3 shows a simulation of the magnitude of the circular reflection coefficients for sea water presented as co-polarization and cross-polarization components. Values for the dielectric constant ($\epsilon_r = 20$) and conductivity ($\sigma = 4$ S/m) are representative for sea water in the 1 GHz region [Hannah, 2001].

When the co- and cross-polarization components are different in magnitude the resulting polarization is elliptic, whereas when they are equal (at the Brewster angle at about 8°) the resulting polarization is

linear. Keeping this concept in mind when looking at Fig. 3 it can be seen that for angles lower than the Brewster angle the original signal component (RHCP) is predominant and hence the result is Right Hand Elliptical Polarization. For angles greater than the Brewster angle the predominant signal component is the cross polarization (LHCP) resulting in Left Hand Elliptical Polarization, until reaching an elevation angle of 90° where the polarization becomes fully LHCP.

Another point to make from Fig. 3 is that the magnitude of the LHCP component of the reflected signal is always lower than the RHCP signal before reflection. Furthermore, the magnitude of the cross-polarization component increases rapidly between 0° to 20° of elevation and stabilizes after 40° to the value 0.8. This increase should be directly visible in the signal-to-noise-ratio (SNR) of the reflected signal, compared with the SNR of the direct signal, in the GNSS-based tide gauge installation.

2.2. Reflective surface

The reflection off the sea surface has so far been considered to originate from a single geometric point (specular point) on the surface. However, since a GNSS satellite illuminates a large region of the Earth, reflections from parts of this area (surrounding the specular point) will contribute to the total reflected signal. This can be described by specular reflection, meaning a plane wave field reflected in a perfectly flat surface. The reflected signal power is coherent and the reflective surface can be described by the first Fresnel zone with the specular point in the center, see e.g., Beckmann and Spizzichino [1987]. The first Fresnel zone is defined by a phase change of the signal, across the reflective surface, of less than half the signal wavelength. From this, the semi-major axis (a) and the semi-minor axis (b) of the first Fresnel zone (or ellipse) can be calculated as

$$a = \frac{\sqrt{\lambda h \sin \epsilon}}{\sin^2 \epsilon}; \quad b = \frac{\sqrt{\lambda h \sin \epsilon}}{\sin \epsilon} \quad (2)$$

where λ is the wavelength, h is the height of the receiving antenna over the reflector, and ϵ is the elevation angle of the satellite.

When the surface roughness increases, the reflected signal will spread in space, i.e., the incoherent part of the reflected signal increases and the coherent part decreases. Additionally, for rough surfaces, the area of reflections extends into a glistening zone surrounding the specular point, see e.g., Cox *et al.*

[1954]. However, for smooth enough surfaces, the area of the first Fresnel zone is still the major contributor to the total reflected energy and can be used as an approximation of the reflective surface.

From Eq. 2 it is possible to simulate the reflective surface (area of an ellipse, $ab\pi$) for different satellite elevation angles and antenna heights over the sea surface. The simulation is shown in Fig. 4, where the area (in m^2) of the reflective surface is presented in a contour plot. The elevation angle shown is limited to between 20° and 80° where the upper limit is due to satellite visibility at the GNSS-based tide gauge site (at 57° N there are no GNSS satellites visible above 80°). The lower limit comes from the fact that the magnitude of the LHCP reflection coefficient is low for lower elevations (0 to 0.7 for elevations below 20° , see Fig. 3). This means that the SNR of the reflected signal (received through the LHCP antenna) is much lower for elevations below 20° , compared to elevation above 20° , and therefore disregarded in our data analysis.

It is clear from Fig. 4 that a decrease in elevation angle or an increase in antenna height corresponds to an increased size of the reflective surface. This results in large reflecting surfaces for low elevations, e.g., at elevation 1° the reflective surface is between 500 and 2500 m^2 (not shown in here). What can also be seen is that a decrease in antenna height decreases the size of the reflective surface where, e.g., for an antenna height of about 1 to 3 m the reflective surface is relatively small, not extending 10 m^2 .

Not only the size of the reflective surface area is of interest, but also its shape (elliptic) and orientation. The semi-major axis of the elliptic surface extends in the same direction as the vector from the sub-satellite point to the receiving antenna and is therefore continuously moving with the satellite. The ellipticity is only dependent upon the elevation angle and goes from 0 (circular) to 1 (extending to infinity) as $e = \cos(\varepsilon)$. This means that for higher elevations the reflective area is nearly circular and close to the antenna, whereas for lower elevations the area is highly elliptical extending far away from the antenna.

For the GNSS-based tide gauge the observations are available from multiple satellites with different elevation and azimuth directions. This means that for each epoch, the total reflective surface consists of the area from several ellipses in different sizes distributed over the sea surface. If the height of the

antenna over the sea surface is low (1 to 2 m), the size of the combined reflective surface is small (up to 5 m^2 per satellite, see Fig. 4). Hence, the GNSS-based tide gauge measurement will be more affected by extreme observation values than, e.g., a stilling well gauge, which works as a low-pass filter disregarding high frequency variations of the sea surface. If desired, this effect can be mitigated by increasing the antenna height, which in turn will increase the combined reflective surface.

2.3. Receiver performance

As previously mentioned, when the sea surface roughness increases the coherent part of the reflected signal decreases. At a certain surface roughness, the coherent part of the reflected signal will be too small for the receivers' tracking loop to distinguish from the noise, hence the receiver will lose track of the satellite signal. As an example the number of GPS L_1 phase observations, stored by the receiver connected to the downward-looking LHCP antenna, versus the wind speed (which is correlated with sea surface roughness) is shown in Fig. 5. The GPS observations are taken from 1 Hz-sampled Receiver INdependent EXchange format (RINEX) files [Gurtner and Estey, 2005] during 4 days (October 3, 4, 8, and 9, 2010) and the number of observations are summarized every 10 minutes.

In Fig. 5 there is a clear separation between low wind speeds (4 to 6 m/s) resulting in a high number of observations (~ 4500) and high wind speeds (10 to 12 m/s) resulting in a lower number of observations (~ 2000). This means that the receiver hardware and its internal firmware are limiting factors for the GNSS-based tide gauge.

3. Installation

The experimental setup of the GNSS-based tide gauge was installed temporarily at OSO (about N $57^\circ 23.5'$, E $11^\circ 55.1'$) in September 2010, see Fig. 6. The installation was built on a wooden deck secured on the coastal bedrock, with the antennas extending about 1 m over the coast line. Since the visibility of satellites to the north is limited at these latitudes (57° N), the installation was positioned towards the south with open sea water in a southward direction (from azimuth 40° to 260°) in order to maximize the number of reflections. The antennas were aligned horizontally (see Section 2), and the

downward-looking antenna was positioned approximately 1.5 m over the sea surface at the time of installation. This was done in order to warrant against weather and surf related damage to the installation as tides and waves might crest at 1.2 m above mean sea level (local tidal range ~ 20 cm).

Data were collected during three months in 2010 from September 16 (00:00:00 UTC) to December 19 (23:59:59 UTC). The equipment used was two Leica GRX1200 GNSS receivers, each connected to a Leica AR25 multi-GNSS choke-ring antenna protected by a hemispherical radome (see Fig. 6). Both receivers recorded continuous data with 1 Hz sampling during the entire campaign.

4. Data Processing

An in-house software for relative positioning was developed in MATLAB by *Löfgren et al.* [2011] to analyze the data from the GNSS-based tide gauge in post-processing with broadcast ephemerides [*Dow et al.*, 2009]. This software was further developed into a semi-automated processing scheme that has the possibility to manage large data sets and output results (vertical baseline between the upward and downward antenna) with high temporal resolution, i.e., every 10th minute. The core part of the software uses standard geodetic processing, currently for GPS L₁ phase delays, for single differences according to

$$\lambda \Delta \Phi_{AB}^j(t) = \Delta \varrho_{AB}^j(t) - \lambda \Delta N_{AB}^j + c \Delta \tau_{AB}(t) \quad (3)$$

where λ is the wavelength of the GPS L₁ carrier, $\Delta \Phi_{AB}^j(t)$ are the measured carrier phase differences between the two receivers expressed in cycles, $\Delta \varrho_{AB}^j(t)$ are the differences in geometry, ΔN_{AB}^j are the phase ambiguity difference in cycles, c is the speed of light in vacuum, and $\Delta \tau_{AB}(t)$ are the receiver clock bias differences. The equation is expressed in meters and subscripts A and B denote the two receivers, superscript j denotes the satellite, and t denotes the epoch. Both tropospheric and ionospheric effects were left out in Eq. 3, since the baseline between the receivers was short and we can assume that these effects cancel out by single differencing.

Expanding the term for the difference in geometry, it is possible to use azimuth α and elevation ε for each satellite and express them in a local coordinate system as

$$\Delta \varrho_{AB}^j(t) = \Delta e \sin(\alpha^j) \cos(\varepsilon^j) + \Delta n \cos(\alpha^j) \cos(\varepsilon^j)$$

$$+ \Delta v \sin(\varepsilon^j) \quad (4)$$

where Δe , Δn , and Δv are the east, north, and vertical components of the baseline between the two receivers, respectively. Since the horizontal baseline is zero (see Section 3), both the east and north component can be disregarded in our processing.

Using multiple satellites during several epochs results in multiples of Eq. 3, which then can be expressed as the following linear system of equations

$$Dx = y + \epsilon \quad (5)$$

where y is a vector of observed single differenced phase measurements; D is the design matrix containing partial derivatives for the vertical baseline, phase ambiguity differences for each satellite pair, and differences in receiver clock bias; x is a vector containing the estimated parameters (vertical baseline, phase ambiguity differences, and differences in clock bias); ϵ contains the unmodeled effects and measurement noise.

Before the processing, an elevation and azimuth mask was applied to the data. The azimuth mask extended from 40° to 260° azimuth, removing unwanted observations from the north-northeast (this northern area consists of bedrock and coast line). The elevation mask removed observations with elevations below 20° . This limit was set because of the low SNR of the reflected signals received from low elevations (see Section 2.1).

After adjusting the differential observations for time-tag bias effects on the measured pseudoranges (see e.g., *Blewitt* [1997]), Eq. 5 was solved with a least-squares analysis for every 10 minutes using overlapping data intervals of 20 minutes for each solution. Every solution included the vertical baseline component for the current interval, phase ambiguity differences for each satellite pair for the current interval, and receiver clock differences for each epoch. The conditions on each solution were that both receivers had continuous track of the same satellites for at least 10 minutes during the interval and that there were at least 2 satellites visible at each epoch.

The solutions of vertical baseline between the upward and downward-looking antennas were converted into a time series of local sea level, relative to the LHCP antenna, using Eq. 1. However, the vertical distance between the antenna phase centers where not accounted for, which will cause a bias.

Phase center corrections were not applied in the processing. This is not a major concern, since for el-

evations above 20° the maximum difference between two observations in two different azimuth direction never exceed 1.5 millimeter, see Section 2 and Fig. 2.

In order to remove erroneous sea-level solutions, all solutions with standard deviation (i.e., the formal error in the least-squares minimization process) larger than 1 cm were disregarded. This approach resulted in remaining solutions for 60.3% of the intervals (8245 of a total of 13680 intervals) during the three months. We found that 2.4% of the solutions in the created sea-level time series were based on observations of 2 satellites only, while 83.2% of the solutions were based on observations of at least 4 satellites.

5. Time Series of Local Sea Level

The GNSS-derived time series was compared to independent sea-level observations from two stilling well gauges operated by the Swedish Meteorological and Hydrological Institute (SMHI) at Ringhals and Gothenburg about 18 km south and 33 km north of OSO, respectively. All time series for 3 months (or 95 days) are presented together in Fig. 7 where a mean is removed from each time series. This was done because the GNSS-derived sea level is relative to the LHCP antenna, whereas the SMHI sea-level observations are relative to the mean sea level of the year [Hammarklint, 2010].

The GNSS-derived time series consists of solutions every 10 minutes starting at the full hour (see Section 4), whereas the conventional sampling rate of the high resolution SMHI stilling well gauge time series (which is also 10 min) starts at 5 minutes past the full hour and incorporated values of even higher sampling rate [Hammarklint, 2010].

In Fig. 7 the GNSS-derived sea level resembles the variations from the sea-level observations from the nearby stilling well gauges. The sea-level estimates track the peaks in the sea-level observations, e.g., beginning of November 12 and middle of November 28, and also fluctuations during calmer periods, e.g., September 26 to October 1 and October 7 to 17. However, the GNSS-derived time series is more noisy than the stilling well gauge time series and there are also a few outliers most probably originating from too few observations and/or bad satellite geometry. Furthermore, there are periods where there are no sea-level solutions available from the GNSS-based tide gauge processing, e.g., October 2 to 6. This

is in general attributed to both software restrictions and the receivers' capability of keeping lock on the reflected satellite signals (see Section 2.3).

Finer features of the sea-level time series can be distinguished; Fig. 8 shows a zoom into Fig. 7 during three days from October 13 to 15 as an example. Here all three time series are presented together with the standard deviation for the GNSS solutions (the formal error in the least-squares minimization process) multiplied by a factor of 10. The diurnal signals in Fig. 8 suggests the impact of the local ocean tides at each of the tide gauge stations.

6. Sea-Level Analysis

In order to investigate how well the GNSS-derived local sea level agrees with the SMHI sea-level observations from the stilling well gauges at Ringhals and Gothenburg, a closer comparison is necessary. Since all tide gauges are positioned along the same coast line (at the Kattegatt), the first step is to compare them directly in the time domain. The second step in the comparison is a spectral comparison of the time series, investigating the coherence spectra and the cross-covariance of the time series. The third and last step of the analysis is to examine which tidal constituents that can be resolved from the GNSS-derived and the stilling well gauge sea-level time series.

6.1. Time domain comparison

Time domain comparisons were done between the GNSS-derived sea-level time series and both stilling well sea-level observations. First, to ensure simultaneous data, the stilling well time series were linearly interpolated to the time tags of the GNSS-based time series. This means time tags every 10 minutes starting at the full hour. The longest time interval for interpolation was 5 minutes (10 minutes between original values). However, since there were even more frequent values in the SMHI time series, the interpolation interval was sometimes shorter. The mean of the interpolated stilling well time series were then removed to avoid biases from the interpolation.

The correlation between the time series were investigated through scatter plots of the GNSS-derived sea level and the interpolated Ringhals and interpolated Gothenburg time series (Fig. 9a and Fig. 9b, respectively) and of the both interpolated stilling well gauge time series together (Fig. 9c). The sea-level data are presented as dots and $x = y$ is shown

as a dashed line. Slope coefficients (β) for the combinations were determined using a least-squares fit, and are presented as lines, and correlation coefficient (ρ) are presented for each combination.

The correlation between the GNSS-derived sea level and the sea level from the two stilling well gauges is high with correlation coefficients equal or higher than the correlation coefficient for Ringhals and Gothenburg together (0.95, 0.96, and 0.95, respectively). Furthermore, the slope coefficients for OSO versus Gothenburg and Ringhals versus Gothenburg are close to 1.0, which can be seen in Fig. 9b and Fig. 9c where the $x = y$ line is hard to distinguish behind the slope. The slope coefficient for OSO versus Ringhals is slightly lower (0.90).

The pairwise mean (absolute), maximum, and Root-Mean-Square (RMS) differences in local sea level were calculated for the different time series and are presented in Tab. 1. The mean and RMS values from the GNSS-derived time series are lower than for the two stilling well gauges together. This is an indication that the GNSS-based tide gauge gives meaningful and valuable results. However, the difference in mean and RMS values can be partially explained by the longer geographical distance between the stilling well gauge sites. It is also clear from Tab. 1 that there are larger outliers in the GNSS-derived time series.

6.2. Spectral analysis

In the cross-spectrum analysis we started with estimating the covariance of the three pairs (1) GNSS-based tide gauge at OSO versus Ringhals, (2) GNSS-based tide gauge at OSO versus Gothenburg, and (3) Gothenburg versus Ringhals. Since we are interested in wide-band features of the interrelations, the tidal signals as determined in the harmonic analysis (see Section 6.3) were subtracted.

Figure 10a and Fig. 10b shows the coherence spectra for OSO versus Ringhals and OSO versus Gothenburg, respectively. Both spectra show high coherence with distinct features around 0.4-0.7 cycles per day (local frontal weather patterns), distinct semi-diurnal tides (2 cycles per day) and higher frequency features up to 6 cycles per day.

Using the cross-covariance we also estimated a Wiener filter by down-weighting the cross-spectrum with the coherence spectrum and windowing to ± 128 samples for smooting. The Wiener filter gain is shown in Fig. 11. In the construction of the Wiener

filter there is a loss of long-period signal due to the tapering, in the present cases at the order of 10%. For this reason the gain spectrum was adjusted by adding the spectrum of the 128-point window scaled with the loss with respect to the untruncated gain spectrum at frequency zero. This operation affects the first 10 frequency bins of the Wiener filter spectrum. The operation is equivalent to adding a Heaviside function to the step response of the filter such that their asymptotic value at the largest positive lag is equal to the raw step response.

With the filters thus constructed (see Fig. 11), a prediction of e.g. the sea level of Ringhals from the sea level at Gothenburg explains 75% of the signal. The Wiener filter spectrum shows a knee that appears to depend linearly on the distance and represents approximately the relation

$$d = \frac{1}{2} \omega_{knee} \sqrt{g\bar{H}} \quad (6)$$

where d is the distance between the station and \bar{H} the average depth (25 m in this part of Kattégatt; the lower bound of the group velocity of gravity waves in shallow water is implied, $2c_{gr} \geq c = \sqrt{g\bar{H}}$, see Krauss [1973]). The formula gives a knee frequency of 6 cycles per day for a distance of 50 km.

6.3. Ocean tide analysis

The harmonic parameters of some of the major tide waves at the three tide gauges shown in Table 2 were computed on the basis of the *Tamura* [1987] tide potential development. Data sections of one year (2010) sampled at 600 s were used in the case of the SMHI stilling well gauges, and all available data from the GNSS-based tide gauge (95 days). In the latter case, outlier editing was applied resulting in a rejection of 20 samples that exceeded a 5σ threshold.

Table 2 presents a comparison of the GNSS-based tide gauge at OSO with the stilling well gauges at Gothenburg and Ringhals. First of all, we find meaningful tide parameters with the GNSS-based tide gauge. The values are in between those for the Gothenburg and Ringhals sites. Because of its noise, the GNSS-based tide gauge permitted determination above 1σ of a few major species only: M_2 , S_2 , N_2 , O_1 , and M_4 . The latter is generated by nonlinear response of the basin to the principal lunar tide M_2 .

Results for a small range of different tide waves are collected in Tab. 2. Our tide gauge results also point to major problems with global tide models in Kattégatt as evident in Tab. 3 and Tab. 4. The mod-

els we have chosen are FES2004 [Letellier, 2004] and TPXO.7.2 [Egbert and Erofeeva, 2002], a recalculation of the TPXO suite from Oregon State University [Egbert et al., 1994]. The solutions for the two major constituents, M_2 and O_1 , show large differences as far west as in Skagerak. However, as we shall see below, TPXO.7.2 provides more suitable boundary values in Skagerak when we employ local high-resolution models of Kattegatt as becoming evident in Tab. 3 and Tab. 4.

Directing our attention to the detection of the quarter-diurnal wave M_4 , we notice an intermediate position between the harmonic constants at Ringhals and Gothenburg also for this wave. The M_4 is a so-called nonlinear tide since most of its energy is a by-product of the nonlinear response of a basin to the principal tide M_2 . Our result is particularly interesting to investigate further, since global models for the M_4 tide are rare, and thus limit the reconciling of our tide gauge results with existing models. The FES2004 model does include the M_4 tide. However, comparing the solutions for the principal tides in Kattegatt with e.g. TPXO.7.2 and our own modelling efforts, it appears that FES2004 carries over much of the North Sea response from the west side of the Danish mainland to the east side, potentially due to interpolation and/or smoothing over a distance range that is much too wide for the dimensions of the Jutland peninsula.

Noting the limitations of FES2004 (accuracy) and TPXO.7.2. (resolution) a time-stepping tide model has been employed to predict the tides of Kattegatt, fully furnished to include nonlinearity from three different sources (bottom friction, shallow water, and advection). The model is indeed able to reproduce M_4 amplitudes at the examined section of the coast at the observed order of magnitude of 10 mm.

The time-stepping ocean tide solver is an in-house product that iterates the shallow-water equations in the barotropic approximation; documentation is available at <http://froste.oso.chalmers.se/hgs/OTEQ/>. A few details to be mentioned here: We used a finite-difference scheme with 2 km mesh width, essentially a tangential-plane grid, however with Coriolis acceleration computed at each grid node separately. Bathymetry from ETOPO1 [Amante and Eakins, 2009] was used. The time step, 23 s, was 0.95 subcritical, the length of the series from which harmonic solutions were obtained, covered seven months. The basin was excited with eleva-

tion values from the TPXO7.2 tide model [Egbert and Erofeeva, 2002] at a north-south running boundary through Skagerak (roughly from Hanstholm, Denmark, to Arendal, Norway). We deduced the 40 most significant tide species from the 11 species given in TPXO.7.2, interpolating in the response spectrum (long-period, diurnal, and semi-diurnal). Inside the basin, the tide generating potential from Tamura [1987] was used, again comprising of 40 waves, and ocean loading effects from the world ocean have been added. The self-attraction and -loading effects were parametrised (assuming a coefficient of 0.02 as an effective mean of the loading Greens function pertaining to the Love number combination $1+k'_n-h'_n$). See Tab. 5 for our M_4 results, where model calculations were performed with different friction coefficients q . We found that the largest internal generation of nonlinear M_4 occurred in a model with advection neglected and very low bottom friction, hinting at the relative importance of the shallow-water formulation.

This model produced M_2 amplitudes of twice the height of the observed ($M_4:M_2$ ratio of 0.014 at Onsala). Models with higher friction reproducing the observed of magnitude at M_2 came up with much reduced $M_4:M_2$ ratios, 0.005 or less. However, using FES2004, at the Skagerak boundary, the results change radically. FES2004 includes an M_4 tide, and the Kattegatt basin appears to co-oscillate efficiently. In Fig. 12 we show the tidal chart of this variant. However, the OTEQ/FES2004 solution is still not satisfactory for the part of its phase patterns. This lends us to return a question as to how realistic FES2004 predicts M_4 in Skagerak.

The modelling results in Tab. 3 and Tab. 4 designated by “MSB” are variants of a $0.005^\circ \times 0.005^\circ$ adaption of the model code of Egbert and Erofeeva [2002] to Kattegatt. This model solves the Laplace tidal equations in the frequency domain, which implies that it inherently linearizes the ocean tide problem. The variants differ in their boundary values that have been interpolated on the grids of a suite of global tide models, EOT08a [Savcenko and Bosch, 2008], GOT4.7 (a recent member of the Goddard Ocean Tide model family, Ray [1999]), and the aforementioned models FES2004 and TPXO7.2.

7. Conclusions and Outlook

The time series of sea level from the GNSS-based tide gauge at the Onsala Space Observatory (OSO)

show good agreement with the independently observed sea-level data from the stilling well gauges at Gothenburg and Ringhals. The GNSS-derived sea level is more noisy with some outliers, but the root-mean-square difference in comparison with the stilling well gauges, 5.9 cm and 5.5 cm, is still smaller than for the two stilling well gauges together, 6.1 cm. The comparison is affected by local variations in sea level and systematic effects due to the different techniques, but still shows that the GNSS-based tide gauge gives meaningful and valuable results.

Data gaps in the GNSS-based tide gauge results are related to high wind conditions, i.e. rough sea, indicating limitations of the receiver that is connected to the downward-looking antenna.

The comparison to the stilling well tide gauge observations shows a high level of agreement in the time and frequency domain. The data sets are coherent up to a frequency of six cycles per day. We successfully derived significant amplitudes and phases of some major tides from the GNSS-based time series, e.g., the amplitude of the M_2 and O_1 tides are determined with 1σ uncertainties of 11 mm and 12 mm, respectively. The agreement with ocean tidal results from the stilling well gauges is reasonable, and the OSO results are in between those for the Gothenburg and Ringhals sites. Comparison to model calculations based on global ocean models and local refinement reveals accuracy limitations of the global ocean tide models. In particular it is a challenge to reproduce the observed amplitudes and phases of the M_4 tide by model calculations.

We are currently installing the GNSS-based tide gauge permanently at OSO. Additionally, we plan to supplement it with a pressure sensor tide gauge at the same site. This will allow to closely monitor the sea level at OSO and to compare the different techniques with the same temporal resolution, coastal geometry, and hydrological conditions. For the future, our aim is to develop strategies for real-time sea-level monitoring.

An important future task is to reduce the amount of data gaps in the time series. We have shown that the receiver connected to the downward-looking antenna, receiving the reflected signals, to some extent is limiting the number of observations. However, there is still room for improvements, since so far only GPS signals were analyzed. Adding GLONASS observations, and in the future GALILEO observations, in the processing will provide a higher number of ob-

servations per epoch. This will in turn increase the number of solutions and improve the results.

Furthermore, by changing the processing technique into a filter-based processing scheme, e.g., Kalman filter, the processing speed would reduce substantially and possibly allow more flexible solution windows and an increase in solutions. This means that by developing the software, parts of the data gaps can be avoided. Additionally, we work on an improved handling of phase center variations, cycle slips, and phase ambiguities.

Acknowledgments. We would like to thank the Swedish Meteorological and Hydrological Institute for providing stilling well gauge data from the sites at Gothenburg and Ringhals. The equipment used for the GNSS-based tide gauge (receivers, antennas) were purchased via the Leica Geosystems ATHENA program. Finally, we would also like to thank Adlerbertska Forskningsstiftelsen for partially funding this project.

References

- Amante, C., and B. W. Eakins, (2009), ETOPO1 1 Arc-Minute Global Relief Model: Procedures, Data Sources and Analysis, *NOAA Technical Memorandum NESDIS NGDC-24*.
- Anderson, K., (2000), Determination of water level and tides using interferometric observations of GPS signals, *J. Atmos. Ocean Tech.*, 17(8), 1118–1127.
- Beckmann, P., and A. Spizzichino, (1987), *The Scattering of Electromagnetic Waves from Rough Surfaces*, Artech house, Norwood, USA.
- Belmonte Rivas, M., and M. Martin-Neira, (2006), Coherent GPS reflections from the sea surface, *IEEE Geosci. Remote Sens. Lett.*, 3, 28–31.
- Bindoff, N. L., J. Willebrand, V. Artale, A. Cazenave, J. Gregory, S. Gulev, K. Hanawa, C. Le Qur, S. Levitus, Y. Nojiri, C. K. Shum, L. D. Talley, and A. Unnikrishnan, (2007), Observations: Oceanic Climate Change and Sea Level, In: *Climate Change 2007: The Physical Science Basis*. Contribution of Working Group I to the Fourth Assessment Report of the Intergovernmental Panel on Climate Change [Solomon, S., D. Qin, M. Manning, Z. Chen, M. Marquis, K. B. Averyt, M. Tignor and H. L. Miller (eds.)], Cambridge University Press, Cambridge, United Kingdom and New York, NY, USA, pp. 385–432.
- Blewitt, G., (1997), Basics of the GPS Technique: Observation Equations, In: *Geodetic Applications of GPS*, [Johnson B. (ed.)], Nordic Geodetic Commission, Sweden, ISSN 0280-5731, 10–54.
- Caparrini, M., A. Egado, F. Soulat, O. Germain, E. Farres, S. Dunne, and G. Ruffini, (2007), Oceanpal@: Monitoring Sea State with a GNSS-R Coastal Instrument, *Proceedings of the 2007 IEEE International Geoscience and Remote Sensing Symposium*, July 23–28 2007, Barcelona, Spain, 5080–5083.
- Cox, C., and W. Munk, (1954), Measurements of the roughness of the sea surface from photographs of the Sun's glitter, *J. Opt. Soc. Am.*, 44, 838–850.

- Dow, J. M., R. E. Neilan, and C. Rizos, (2009), The International GNSS Service in a changing landscape of Global Navigation Satellite Systems, *J. Geod.*, 83, 191–198.
- Egbert, G. D., A. F. Bennett, and M. G. G. Foreman, (1994), TOPEX/POSEIDON tides estimated using a global inverse model, *J. Geophys. Res.*, 99(C12), 24821–24852.
- Egbert, G. D., and S. Y. Erofeeva, (2002), Efficient inverse modeling of barotropic ocean tides. *J. Atmos. Oceanic Technol.*, 19, 183–204.
- Gleason, S., S. Hodgart, Y. Sun, C. Gommenginger, S. Mackin, M. Adirad, and M. Unwin, (2005), Detection and Processing of Bi-Statically Reflected GPS Signals From Low Earth Orbit for the Purpose of Ocean Remote Sensing, *IEEE Transactions on Geoscience and Remote Sensing*, 43(6), 1229–1241.
- Gurtner, W., and L. H. Estey, (2005), RINEX: The Receiver Independent Exchange Format Version 2.11, <ftp://igsceb.jpl.nasa.gov/igsceb/data/format/rinex211.txt>
- Hammarklint, T., (2010), Swedish Meteorological and Hydrological Institute (SMHI), Norrköping, Sweden, personal communication.
- Hannah, B. M., (2001), Modelling and simulation of GPS multipath propagation, *Ph.D. thesis*, Queensland University of Technology.
- Krauss, W., (1973), *Methods and Results of Theoretical Oceanography—I. Dynamics*, Gebr. Borntraeger, Berlin.
- Letellier, T., (2004), *Etude des ondes de mare sur les plateaux continentaux*, Ph.D. Thesis, Université de Toulouse III, Ecole Doctorale des Sciences de l'Univers, de l'Environnement et de l'Espace, Toulouse, France.
- Lidberg, M., J. M. Johansson, H.-G. Scherneck, and G. A. Milne, (2010), Recent results based on continuous GPS observations of the GIA process in Fennoscandia from BIFROST, *Journal of Geodynamics*, 50(1), 8–18.
- Lowe, S. T., J. L. LaBrecque, C. Zuffada, L. J. Romans, L. E. Young, and G. A. Hajj, (2002), First spaceborne observation of an Earth-reflected GPS signal, *Radio Science*, 37(1), 28 pp.
- Lowe, S. T., C. Zuffada, Y. Chao, P. Kroger, L. E. Young, and J. L. LaBrecque, (2002b), 5-cm-Precision aircraft ocean altimetry using GPS reflections, *Geophys. Res. Lett.*, 29(10), 4359–4362.
- Löfgren, J. S., R. Haas, and J. M. Johansson, (2010), High-rate local sea level monitoring with a GNSS-based tide gauge, *Proceedings of the 2010 IEEE International Geoscience and Remote Sensing Symposium*, 3616–3619.
- Löfgren, J. S., R. Haas, and J. M. Johansson, (2011), Monitoring coastal sea level using reflected GNSS signals, *J. Adv. Space Res.*, *Scientific applications of Galileo and other Global Navigation Satellite Systems*, 47(2), 213–220, doi:10.1016/j.asr.2010.08.015.
- Martin-Neira, M., (1993), A Passive Reflectometry and Interferometry System (PARIS): Application to ocean altimetry, *ESA J.*, 17, 331–355.
- Martin-Neira, M., P. Colmenarejo, G. Ruffini, and C. Serra, (2002), Altimetry precision of 1 cm over a pond using the wide-lane carrier phase of GPS reflected signals, *Can. J. Rem. Sens.*, 28, 3, 394–403.
- Nicholls, R. J., P. P. Wong, V. R. Burkett, J. O. Codignotto, J. E. Hay, R. F. McLean, S. Ragoonaden, and C. D. Woodroffe, (2007), Coastal systems and low-lying areas, In: *Climate Change 2007: Impacts, Adaptation and Vulnerability*. Contribution of Working Group II to the Fourth Assessment Report of the Intergovernmental Panel on Climate Change [Parry, M. L., O. F. Canziani, J. P. Palutikof, P. J. van der Linden, and C. E. Hanson (eds.)], Cambridge University Press, Cambridge, UK, 315–356.
- Ray, R. D., (1999), A global ocean tide model from TOPEX/POSEIDON altimetry: GOT99.2, *NASA Tech. Memo.*, 209478.
- Rees, W. G., (2003), *Physical principles of remote sensing*, second edition, University press, Cambridge, United Kingdom.
- Savcenko, R., and W. Bosch, (2008), *EOT08a, empirical ocean tide model from multi-mission satellite altimetry*, Report No. 81, Deutsches Geodätisches Forschungsinstitut (DGFI), München.
- Scherneck, H.-G., M. Lidberg, R. Haas, J. M. Johansson, and G. A. Milne, (2010), Fennoscandian strain rates from BIFROST GPS: A gravitating, thick-plate approach, *Journal of Geodynamics*, 50(1), 19–26.
- Tamura, Y., (1987), A harmonic development of the tide-generating potential, *Bull. Info. Maries Terrestres*, 99, 6813–6855.
- Zumberge, J. F., M. B. Heflin, D. C. Jefferson, M. M. Watkins, and F. H. Webb, (1997), Precise point positioning for the efficient and robust analysis of GPS data from large networks, *J. Geophys. Res.*, 102, 5005–5017.
- J. S. Löfgren, Department of Earth and Space Sciences, Chalmers University of Technology, Onsala Space Observatory, SE-439 92 Onsala, Sweden. (johan.lofgren@chalmers.se)
- R. Haas, Department of Earth and Space Sciences, Chalmers University of Technology, Onsala Space Observatory, SE-439 92 Onsala, Sweden. (rudiger.haas@chalmers.se)
- H.-G. Scherneck, Department of Earth and Space Sciences, Chalmers University of Technology, Onsala Space Observatory, SE-439 92 Onsala, Sweden. (hgs@chalmers.se)
- M. S. Bos, CIMAR/CIIMAR, Centro Interdisciplinar de Investigao Marinha e Ambiental, Universidade do Porto, Rua dos Bragas 289, 4050-123 Porto, Portugal. (mbos@ciimar.up.pt)

(Received _____.)

8. FIGURES AND TABLES

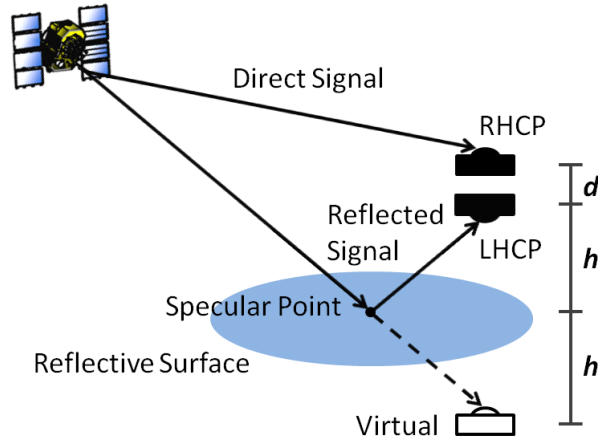


Figure 1. Schematic drawing of the GNSS-based tide gauge concept. A GNSS satellite transmits a Right Hand Circular Polarized (RHCP) signal that is received both directly, by a RHCP antenna, and after reflection off the sea surface by a Left Hand Circular Polarized (LHCP) antenna. When the RHCP signal reflects off the sea surface most of the polarization changes to LHCP. The additional path delay of the reflected signal, as compared to the direct signal, lets the LHCP antenna appear as a virtual antenna located below the sea surface at the same distance (h) as the actual LHCP antenna is located above the sea surface.

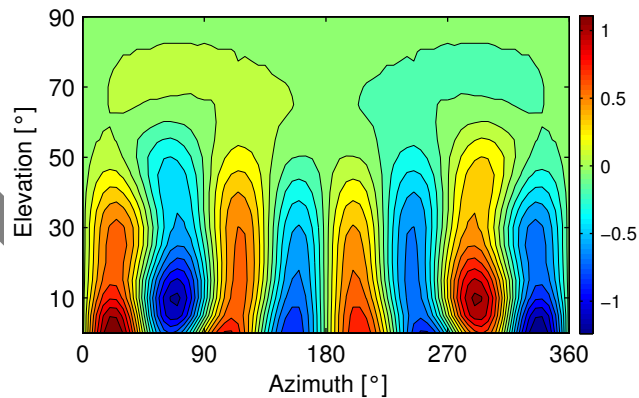


Figure 2. Difference in phase center variations in millimeter between the downward- and upward-looking antenna for the full hemisphere, assuming identical phase center variation patterns for the right hand circular polarized and the left hand circular polarized antenna. Above an elevation of 20° the maximum difference between two observations in two different azimuth directions is less than 1.5 mm.

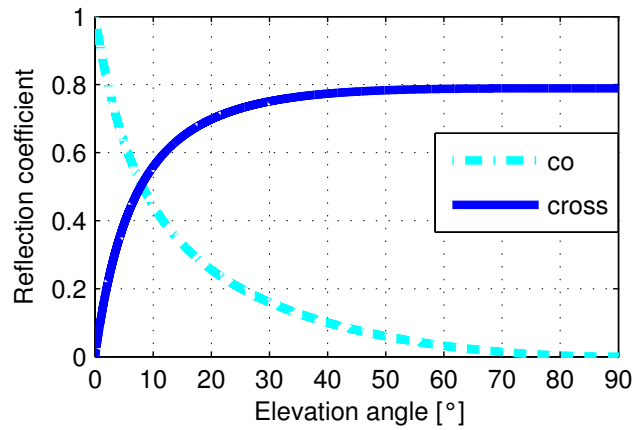


Figure 3. Magnitude of the circular reflection coefficients for specular reflection in sea water at the 1 GHz region represented as co- and cross-polarization components. For angles greater than the Brewster angle (about 8°) the cross-polarization component of the reflected signal predominates.

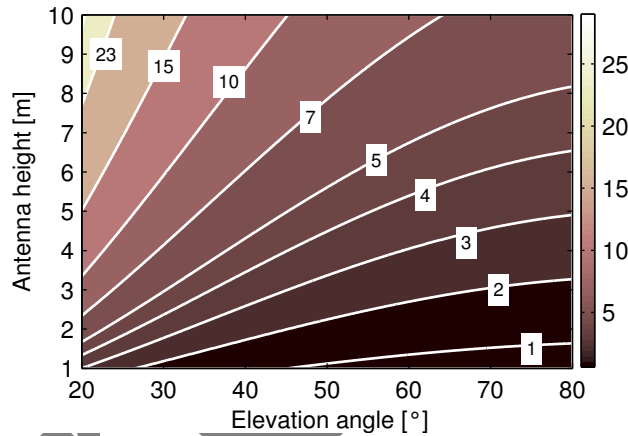


Figure 4. Area of the 1st Fresnel zone (reflective area) in m^2 presented as contours for different satellite elevation angles (20° - 80°) and antenna heights (1 - 10 m) over the sea surface.

Table 1. Pairwise mean (absolute), maximum, and Root-Mean-Square (RMS) differences in local sea level between the GNSS-based tide gauge at the Onsala Space Observatory (OSO) and the stilling well gauges at Ringhals and Gothenburg.

Site 1	Site 2	Mean (cm)	Max (cm)	RMS (cm)
OSO	Ringhals	4.4	55.0	5.9
Gothenburg	OSO	4.0	55.3	5.5
Ringhals	Gothenburg	5.1	35.9	6.1

Table 2. Harmonic solutions for the GNSS-based tide gauge at the Onsala Space Observatory (O), Ringhals (R), and Gothenburg (G) with amplitudes in millimeter and phases in degree, and comparison with a GOTM (Global Ocean Tide Model), FES2004 [Letellier, 2004]. Uncertainty for the tide gauges (one year of observations): amplitude $\pm 0.1 - 0.2$ mm.

Tide	Site	GOTM		Tide gauge		Onsala (GNSS)	
		Amplitude	Phase	Amplitude	Phase	Amplitude	Phase
M2	O	43.1	-153.7			66 \pm 11	145.8
	R	57.6	-132.6	49.0	179.5		
	G	35.3	149.0	72.1	131.0		
N2	O	7.5	9.2			16 \pm 11	125.7
	R	4.3	-30.1	12.5	130.8		
	G	14.0	21.9	18.2	80.5		
O1	O	31.4	-17.8			15 \pm 12	-94.2
	R	38.7	-14.2	22.9	-49.7		
	G	24.9	-28.4	21.3	-65.5		
M4	O	6.8	-148.6			12 \pm 6	-30.7
	R	5.7	-149.5	4.6	-26.7		
	G	8.1	-146.2	9.6	-53.4		
Mf ⁺	O	16.1	-157.4			30 \pm 13	-161.0
	R	16.0	-157.1	18.0	-137.6		
	G	16.4	-157.4	15.3	-130.0		
S2*	O	20.3	55.8			16 \pm 10	102.7
	R	16.1	46.6	7.7	127.8		
	G	25.4	62.6	13.3	82.5		
P1+K1**	O					10 \pm 11	

* The S2 has been analyzed with a different strategy so that the uncertainty for the tide gauge amplitudes is 0.3 mm.

** Uncertainty too high for comparisons

+ Uncertainty for tide gauge amplitudes: 8 mm (Gothenburg), 14 mm (Ringhals)

Table 3. Tide models and GNSS-based tide gauge observations at Onsala Space Observatory. Regional models depend on global models owing to excitation at open-sea boundaries. OTEQ uses a time-stepping finite difference method and non-linear terms, MSB a frequency-domain method and linear approximation. Amplitudes are in millimeters and phases are in degrees.

Model	M ₂		Q ₁	
	Amplitude	Phase	Amplitude	Phase
Global				
FES2004	41.3	-153.7	33.0	-5.8
TPXO.7.2	14.0	57.5	5.4	-17.8
Regional/ excitation				
OTEQ/TPXO.7.2	49.0	139.2	15.5	-47.1
OTEQ/FES2004	65.1	136.4	24.7	1.2
MSB/EOT08a	63.0	155.9	10.6	-2.6
MSB/FES2004	55.2	148.8	13.6	5.7
MSB/GOT4.7	57.1	142.5	11.5	-48.6
MSB/TPXO.7.2*	32.2	150.6	15.0	-50.3
MSB/TPXO.7.2**	31.6	150.6	19.7	-65.7
GNSS Tide Gauge	66	146	15	-94
± Std.dev.	11	10	12	50

* without self-attraction and loading

** with self-attraction and loading

Table 4. Tide models and stilling well gauge observations at Gothenburg. Amplitudes are in millimeters and phases are in degrees.

Model	M ₂		O ₁	
	Amplitude	Phase	Amplitude	Phase
Global				
TPXO.7.2	57.6	97.8	11.6	-58.4
FES2004	35.3	149.0	24.9	-28.5
Regional/ excitation				
OTEQ	66.9	123.9	18.4	-61.1
MSB/EOT08a	76.1	141.6	10.9	-37.7
MSB/FES2004	65.0	137.5	13.3	-26.5
MSB/GOT4.7	74.2	129.3	13.1	-69.9
MSB/TPXO.7.2*	52.2	128.6	16.9	-63.0
MSB/TPXO.7.2**	51.6	128.3	20.2	-71.9
Tide gauge	72.1	131.0	21.3	-65.5
± Std.dev.	1.2	1.0	2.3	6.3

* without self-attraction and loading

** with self-attraction and loading

Table 5. Results for the M₄ tide from the GNSS-based tide gauge at the Onsala Space Observatory (OSO) and the stilling well gauges at Ringhals and Gothenburg. Models versus observations.

Model /excit.	Friction* q [$\times 10^{-3}$]	Gothenburg		OSO		Ringhals	
		Amplitude [mm]	Phase [°]	Amplitude [mm]	Phase [°]	Amplitude [mm]	Phase [°]
OTEQ							
/TPXO.7.2	0.82	1.2	177.6	1.3	155.6	1.3	139.3
/TPXO.7.2	4.10	0.1	-134.7	0.3	-162.5	0.3	-176.8
/FES2004	4.10	8.6	-127.2	6.9	-120.6	5.9	-117.6
Tide gauge		9.6	-53.5	11.7	-31	4.6	-27.0
±Std.dev.		0.6	3.3	6.6	34	0.7	8.3

* Friction law: $\mathbf{M}_{t+1} = \mathbf{M}_t + q \Delta t |\mathbf{U}_t| \mathbf{U}_t + \text{other forces}$, where \mathbf{M} is the mass transport vector and \mathbf{U} velocity.

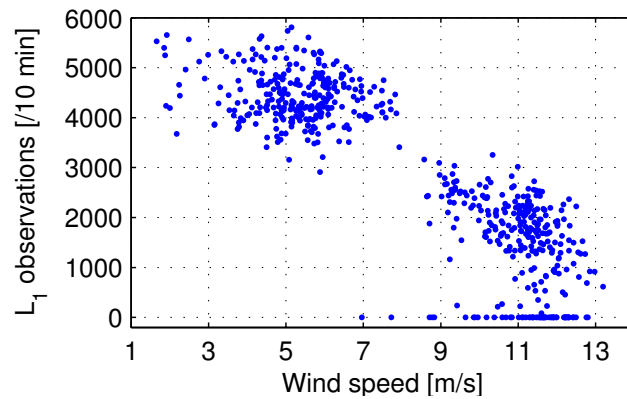


Figure 5. Number of GPS L₁ phase observations per 10 minute interval recorded by the receiver connected to the downward-looking left hand circular polarized antenna versus observed wind speed for 4 days (October 3, 4, 8, and 9, 2010).

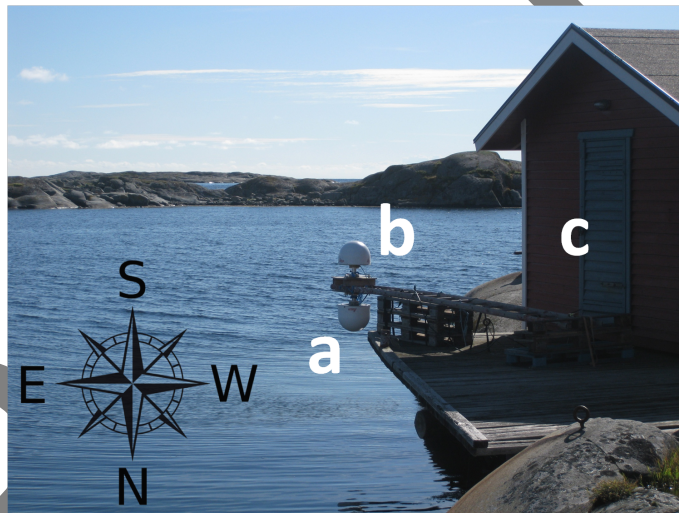


Figure 6. The experimental GNSS-based tide gauge installation at the Onsala Space Observatory consisting of two Leica AR25 choke-ring antennas: one left hand circular polarized (a) and one right hand circular polarized (b). Both antennas are covered with hemispherical radomes and each antenna is connected to a receiver placed in the nearby house (c). The installation is directed towards the south and faces an open sea surface in directions from south-west to south-east. The closest islands in the southern direction are at a distance of more than 100 m from the installation.

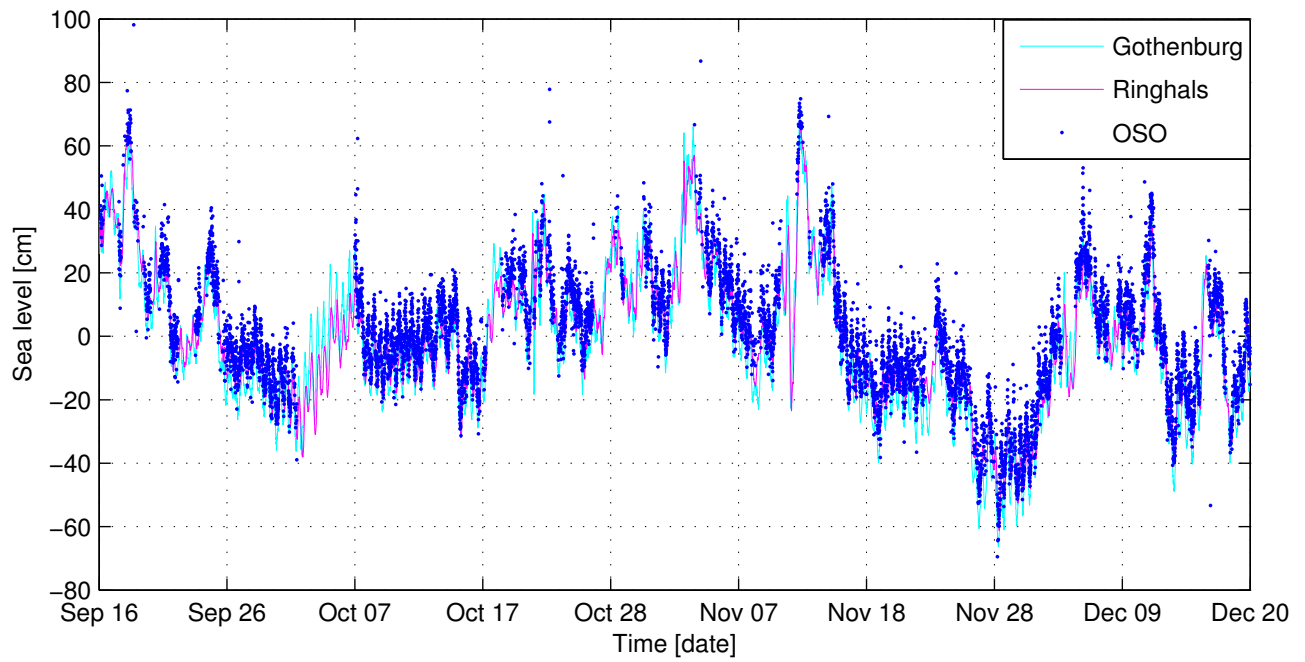


Figure 7. Time series of GNSS-derived local sea level at the Onsala Space Observatory (OSO) for three months (95 days) shown as blue dots together with sea-level observations from two stilling well gauges at Gothenburg (cyan, bright line) and Ringhals (magenta, dark line) about 33 km and 18 km away from OSO, respectively. A mean is removed from each time series.

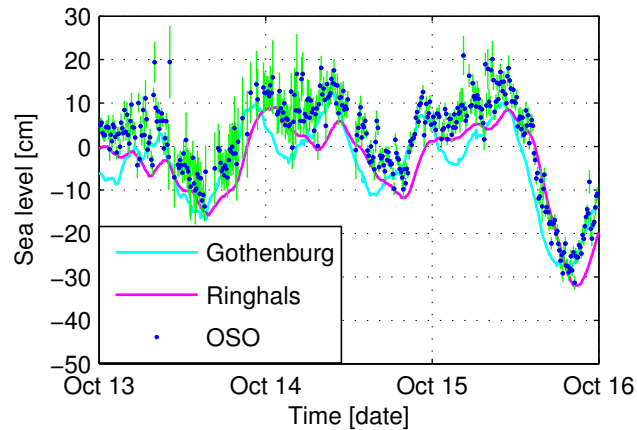


Figure 8. Close-up of three days (October 13 – 15, 2010) of the GNSS-derived local sea level (blue dots) at the Onsala Space Observatory (OSO) and sea-level observations from the two stilling well gauges at Gothenburg (cyan, bright line) and Ringhals (magenta, dark line). Error bars, consisting of standard deviations from each solution multiplied by a factor of 10, are shown for the GNSS-derived time series (green, vertical lines). A mean is removed from each time series.

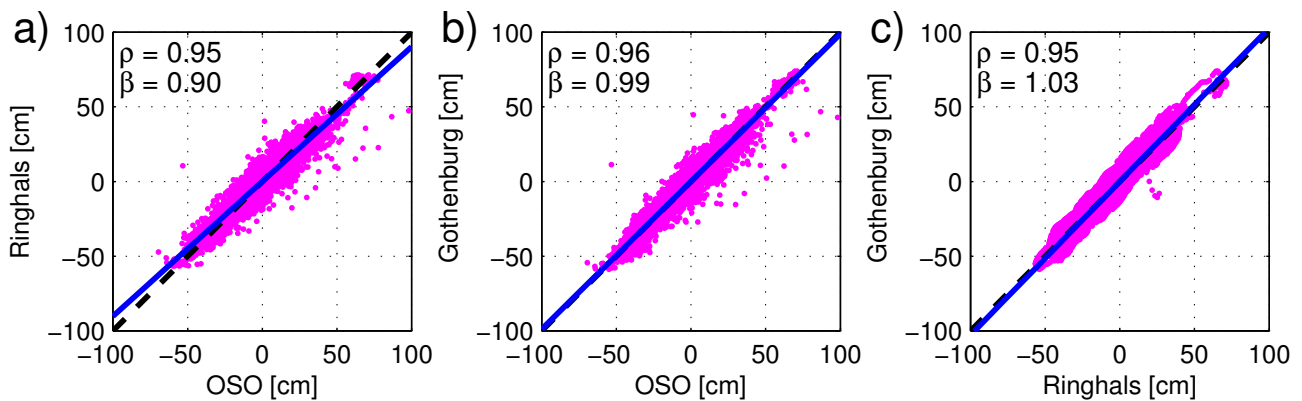


Figure 9. Scatter plots of the sea-level time series showing positive correlation between the GNSS-based tide gauge at Onsala Space Observatory (OSO) and the stilling well gauges at Ringhals (a) and Gothenburg (b), respectively, and between the two stilling well gauges (c). Sea-level data are presented as dots (magenta), $x = y$ lines are shown as dashed lines (black), and least-squares fits of the data are displayed as lines (blue). Correlation coefficients and slope coefficients are indicated by ρ and β , respectively.

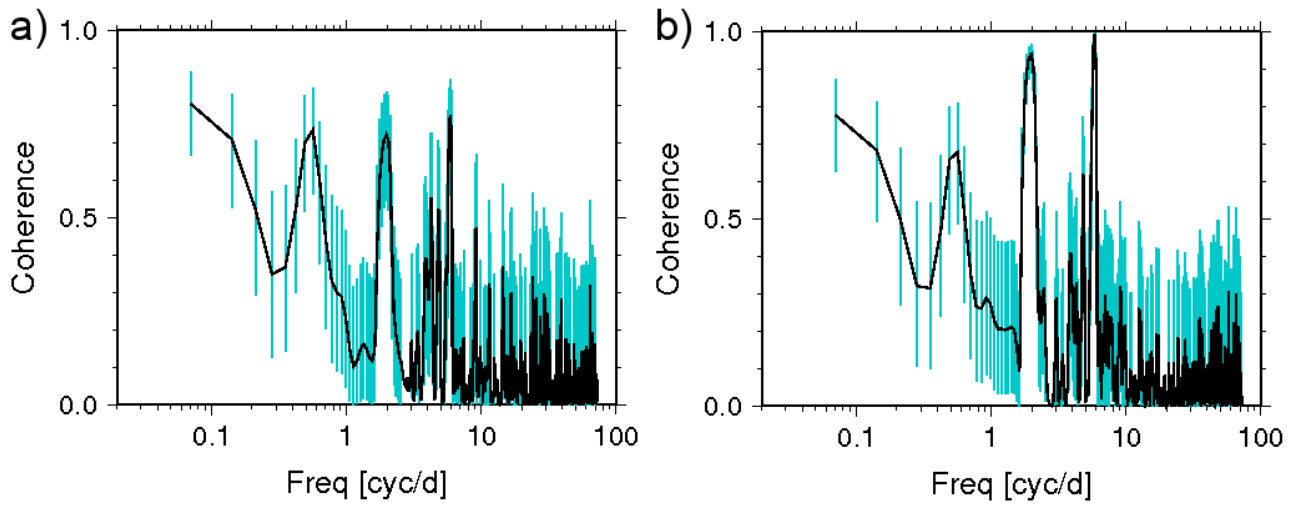


Figure 10. Coherence spectra for the GNSS-based tide gauge at the Onsala Space Observatory (OSO) versus Ringhals and OSO versus Gothenburg. Vertical cyan lines represent 95% confidence intervals.

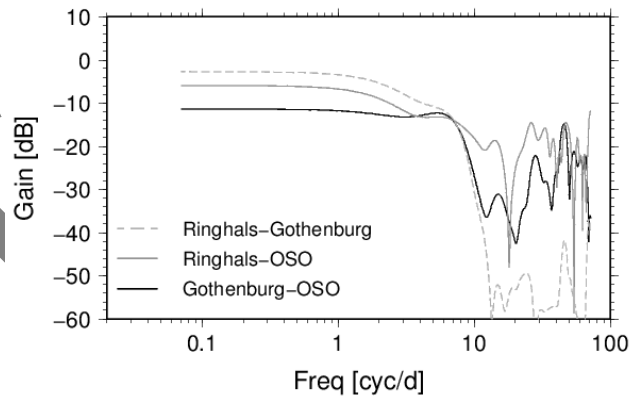


Figure 11. The Wiener filter gain. The knee frequency above which the gain abruptly decreases appears to agree with the frequency of shallow-water gravity waves with wavelengths greater or on the order of the inter-station distance. The attenuated low-frequency gain in the cases of Onsala Space Observatory (OSO) is primarily the consequence of noise in the GNSS-based tide gauge data.

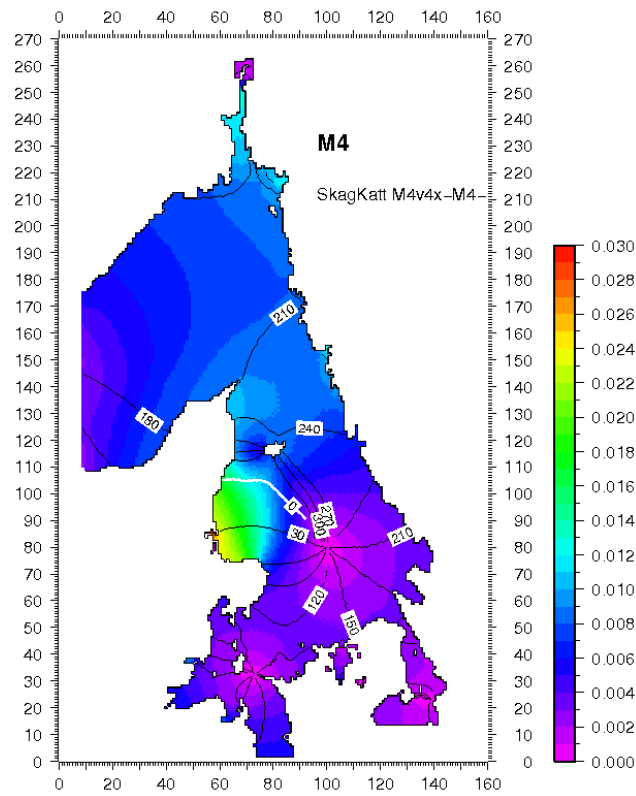


Figure 12. M_4 tide harmonic solution from a nonlinear tide model driven by FES2004. Amplitudes in meters are color coded and phases in degrees are indicated by labeled lines. The boundary values in Skagerak do contain an M_4 tide. Tide phase runs from -118° at Ringhals to -127° at Gothenburg.